Investigation of iron sulfide impact crater residues: a combined analysis by scanning and transmission electron microscopy

P. J. Wozniakiewicz, H. A. Ishii, A. T. Kearsley, M. J. Burchell, P. A. Bland, J. P. Bradley, Z. Dai, N. Teslich, G. S. Collins, M. J. Cole, S. S. Russell

September 23, 2010

Disclaimer

This document was prepared as an account of work sponsored by an agency of the United States government. Neither the United States government nor Lawrence Livermore National Security, LLC, nor any of their employees makes any warranty, expressed or implied, or assumes any legal liability or responsibility for the accuracy, completeness, or usefulness of any information, apparatus, product, or process disclosed, or represents that its use would not infringe privately owned rights. Reference herein to any specific commercial product, process, or service by trade name, trademark, manufacturer, or otherwise does not necessarily constitute or imply its endorsement, recommendation, or favoring by the United States government or Lawrence Livermore National Security, LLC. The views and opinions of authors expressed herein do not necessarily state or reflect those of the United States government or Lawrence Livermore National Security, LLC, and shall not be used for advertising or product endorsement purposes.

Investigation of iron sulfide impact crater residues: a combined analysis by scanning and transmission electron microscopy

Penelope J. Wozniakiewicz[1,2]*, Hope A. Ishii[1], Anton T. Kearsley[2], Mark J. Burchell[3], Philip A. Bland[4,5], John P. Bradley[1], Zurong Dai[1], Nick Teslich[5], Gareth S. Collins[4], Mike J. Cole[3] and Sara S. Russell[2,4].

[1]Institute of Geophysics and Planetary Physics, Lawrence Livermore National Laboratory, 7000 East Avenue, Livermore, CA 94550, USA.

[2]Impacts & Astromaterials Research Centre (IARC), Department of Mineralogy, Natural History Museum, London, SW7 5BD, UK.

[3]Centre for Astrophysics and Planetary Sciences, School of Physical Science, University of Kent, Canterbury, CT2 7NH, UK.

[4]IARC, Department of Earth Science and Engineering, Imperial College London, South Kensington Campus, London SW11 2AZ, UK.

[5]Department of Applied Geology, Curtin University of Technology, GPO Box U1987, Perth WA 6845, Australia.

*Corresponding author: Email: wozniakiewic1@llnl.gov

Abstract Samples returned from comet 81P/Wild 2 by the Stardust mission provided an unequalled opportunity to compare previously available extraterrestrial samples against those from a known comet. Iron sulfides are a major constituent of cometary grains commonly identified within cometary interplanetary dust particles (IDPs) and Wild 2 samples. Chemical analyses indicate Wild 2 sulfides are fundamentally different from those in IDPs. However, as Wild 2 dust was collected via impact into capture media at ~6.1 km s^{-1}, it is unclear whether this is due to variation in pre-accretional/parent body processes experienced by these materials or to heating and alteration during collection.

We investigated alteration in pyrrhotite and pentlandite impacted into Stardust flight spare Al foils under encounter conditions by comparing scanning and transmission electron microscope (SEM, TEM) analyses of pre- and post-impact samples and calculating estimates of various impact parameters. SEM is the primary method of analysis during initial in-situ examination of Stardust foils, and therefore, we also sought to evaluate the data obtained by SEM using insights provided by TEM.

We find iron sulfides experience heating, melting, separation and loss of S, and mixing with molten Al. These results are consistent with estimated peak pressures and temperatures experienced (~85 GPa, ~2600 K) and relative melting temperatures. Unambiguous identification of preserved iron sulfides may be possible by TEM through the location of Al-free regions. In most cases, the Ni:Fe ratio is preserved in both SEM and TEM analyses and may therefore also be used to predict original chemistry and estimate mineralogy.

---

1. INTRODUCTION

Iron sulfides are one of the major mineral types found in cometary dust. They are common in chondritic porous (CP) interplanetary dust particles (IDPs) (Bradley, 2003) and have been identified as a major constituent of the comet 81P/Wild 2 samples collected by NASA's Stardust mission (Zolensky et al., 2006). Iron sulfides in CP IDPs are predominantly pyrrhotite with up to 20 atomic % Ni although occasionally other iron sulfides such as pentlandite, troilite and sphalerite are found (e.g. Fraundorf, 1981; Christoffersen and Buseck, 1986; Zolensky and Thomas, 1995; Dai and Bradley, 2001; Bradley, 2003). In particle analyses from Stardust aerogel impact tracks, the preliminary examination petrology team reported the occurrence of pentlandite (rare) and Ni-free pyrrhotite (Zolensky et al., 2006). However, unlike the CP IDPs

there were no intermediate phases between the iron sulfides and iron-nickel sulfides, and there was a range of non-stoichiometric Ni-free iron sulfide compositions with varying S content (Zolensky et al., 2006). Although the range of S content could be attributed to an original diverse non-stoichiometric composition (and therefore to real differences between CP IDPs and comet 81P/Wild 2), it was also suggested that it could reflect a loss of S as a result of capture heating, thereby indicating the initial impactors were pyrrhotite and pentlandite (Brownlee et al., 2006; Zolensky et al., 2006). Sulfur is considerably more volatile than iron and nickel (based on its 50% condensation temperature, Lodders, 2003) and the mobilization and loss of S from S-bearing minerals upon moderate heating has been previously observed and documented (e.g. Lauretta et al., 1997). In order to ensure correct interpretations of comet 81P/Wild 2 mineralogy, and therefore pre-accretional or parent body processes, an investigation into the effects of capture on sulfides is vital.

The Stardust encounter conditions (well-constrained, relatively low velocity of ~6.1 km s^{-1} and a perpendicular angle of impact incidence, Brownlee et al., 2003) are such that they can be replicated in the laboratory using the two stage light gas gun (LGG). We can therefore take known minerals, impact them into flight spare Stardust collection media and make direct comparisons between the pre- and post-impact materials to determine whether the impactor remains the same or, if not, whether it is even recognizable. Analyses of Stardust aerogel impact analogues of pyrrhotite have previously been undertaken. Using a hard x-ray scanning fluorescence microprobe, spectra were obtained over traverses through a track perpendicular to its length, and S from the pyrrhotite was found to have mobilized and diffused through the aerogel (Ishii et al., 2008a). Of more concern, transmission electron microscopy (TEM) analyses showed that these impacts also resulted in the production of nanometer-sized inclusions of metal and sulfide embedded in a silicate glass (molten aerogel) (Ishii et al., 2008b). This material is almost identical to the CP IDP constituent known as GEMS (glass with embedded metal and sulfides) expected to be found in comet 81P/Wild 2. Therefore, the alteration experienced by sulfides captured in aerogel is not simply the loss of S but is considerably more complex, with the resulting material potentially being indistinguishable from GEMS. Therefore, although larger terminal particles may preserve some sulfide, for the vast majority of aerogel captured grains, deciphering the original mineralogy of sulfides is virtually impossible.

The Al 1100 foils on the Stardust spacecraft had the primary function of securing aerogel blocks in place and allowing their safe removal upon return (Brownlee et al., 2003). However, they also provided an additional capture surface totaling ~153 cm^2 (Tsou et al., 2003) upon which cometary materials may be examined. Unlike the silica aerogel, the material captured by the foils is highly localized in the form of impact residues that line impact craters (Fig. 1). In addition, there is no external source of silicate, and impacts occur into a heat sink rather than an abrasive insulator. The foils therefore have a great potential for providing us with information on impacting cometary grains. In fact, previous investigations into laboratory analogues have already shown that the foils surpass the aerogel in their ability to provide information such as original impactor size, density and structure (e.g. Kearsley et al., 2007, 2008; Burchell et al., 2008a). Analyses of the Stardust cometary impact craters show that they typically contain residues composed of a mixture of crystalline and amorphous materials (Leroux et al., 2008) which are tentatively assumed to be relict cometary dust (crystals) and shock-induced melt that subsequently quenched (amorphous material). Determining the value of these materials to our understanding of comets requires that we understand the impact process and identify the products of capture through analyses of impact analogues. Laboratory analogue analyses suggest precursor chemistry (e.g. Wozniakiewicz et al., 2009) and even crystallinity (Raman signals detected by Burchell et al., 2008b) may be preserved for anhydrous silicate minerals. An investigation into the preservation and/or recognizability of sulfides is the next logical step. A

variety of foils and other surfaces have been exposed in low Earth orbit over the past few decades, successfully sampling materials passing through the local Earth environment. However, the level of preservation varied due to the diverse and unknown impact velocities and angles of incidence. Hence, these findings cannot be used to gain insight into Stardust foils (see Wozniakiewicz et al. (2009), Graham et al. (2001) and Kearsley et al. (2009) for more complete discussion of previous impact crater work). It is the aim of this paper to analyze pre- and post-impact sulfides to determine the state of preservation and extent of alteration, and therefore evaluate the recognizability, of these minerals as collected by Stardust.

The largest Stardust crater identified has a diameter of 680 μm which, according to the particle-crater diameter correlations by Kearsley et al. (2007), would require an impacting particle with a diameter >100 μm. This crater is indeed large compared to the majority of craters on the Stardust foils; however, 63 Stardust craters with diameter >20 μm were identified during the preliminary examination alone, and it is craters of this size that contain the majority of the cometary dust mass collected on Stardust foils (Kearsley et al., 2008). The analyses in this paper therefore focus on craters >50 μm in diameter formed by impacting particles of >10 μm in diameter (Kearsley et al., 2007; Price et al., In Press).

A large array of analytical tools are currently available for mineral analyses (e.g. Zolensky et al., 2000), each presenting different advantages and disadvantages, based on factors that include resolution, ease of sample preparation, speed of analysis, instrument availability, cost, and the extent of sample destruction during analysis. To fully exploit the unique sample set returned by Stardust in its Al foils, the data obtained must be maximized by performing non-destructive, quick, widely available methods to identify samples that might merit further investigation by higher resolution, more laborious and destructive methods. Scanning electron microscopy (SEM) with energy dispersive X-ray microanalysis (EDX) is a widely available technique used extensively to image and perform initial compositional analyses of residues in craters on the Stardust Al foils (e.g. Zolensky et al., 2006; Kearsley et al., 2008). This was the chosen method for initial analysis, and later, for location of residue in our impact analogue foils. TEM is a technique capable of high resolution compositional and structural analyses required for mineralogical classification over the small scales applicable to crater residues. It was therefore used for the more in-depth analyses of the pre- and post-impact samples to identify those features generated by the impact and those inherent to the impactor. These TEM results also allowed us to make a direct practical assessment of the quality of data previously obtained by the SEM. Estimates of the impact parameters (peak pressure, post-shock temperature and cooling time) were calculated to compliment and clarify the findings of these analyses.

2.   SAMPLES AND METHODOLOGY

2.1.   Impact Analogue Production

The sulfide impact analogue foils were generated using the two stage light gas gun (LGG) in the Centre for Astrophysics and Planetary Sciences at the University of Kent, Canterbury. The powder shot and velocity measurement techniques employed here are described in Burchell et al. (1999). In each shot the target chamber was evacuated to a few $\times$ 10^{-1} mbar, or better, to minimize velocity loss in flight.

The target used in each case was a sample of flight-spare Stardust Al foil (provided by P. Tsou of the Jet Propulsion Laboratory). This foil is an Al 1100 series alloy (meeting the specifications of Al 1145) with temper grade 0. The foil is ~101 μm thick (Kearsley et al., 2007) and, for

experimental shots, was wrapped around a 1 mm thick square Al alloy plate (Al 6082) measuring ~1.5 cm x 1.5 cm, to simulate the mounting on the Stardust collector. This was then held with conductive adhesive putty onto an Al base-plate (10 cm x 10 cm), drilled with a hole in each corner for support within the target chamber and to enable handling throughout the shot and subsequent analysis without damage or contamination to the craters and their residues. Throughout this preparation procedure, gloves and pliers were used to avoid contamination of the foil.

The iron sulfides chosen as projectile material were pentlandite and Ni-free pyrrhotite. The pyrrhotite was taken from collections at the Natural History Museum, London (specimen BM.2005,M317 from Drag, Tysfjord, Norway). Available museum samples of pentlandite were generally very small crystals incorporated in larger masses of pyrrhotite, chalcopyrite and pyrite making them impossible to extract without including a high concentration of impurities. These were therefore deemed unsuitable for this investigation and a sample of pentlandite from Sudbury (Ontario, Canada) containing a crystal large enough to extract was purchased from a commercial source. These samples were prepared as projectiles with diameters of 53 μm or less by crushing with a pestle and mortar to produce powders and passing through a 53 μm sieve. Between each projectile the pestle and mortar and the sieve were thoroughly cleaned in order to avoid cross-contamination of different projectiles. The majority of these particles, if they were to reach the target intact, would generate craters at the Stardust upper size limit or greater (based on the particle-crater diameter correlation by Kearsley et al., 2007). However, the acceleration experienced in the LGG is enough to cause sulfide particle break-up, resulting in an array of crater diameters throughout the Stardust range.

Both mineral projectiles were shot individually, generating separate impact analogue foils to ensure any identifications made were associated with the correct mineral. Pyrrhotite was fired in shot G080507#3 at a velocity of 5.82 km s^{-1}. Pentlandite was fired in shots G2205072 and G291106#2 at velocities of 6.21 km s^{-1} and 5.85 km s^{-1} respectively. The average impact speed was 5.96 ± 0.12 km s^{-1} (see Table 1), measured individually in each shot with an accuracy to within 2%.

2.2. Sample Preparation

Samples of the pre-impact projectiles were mounted in resin blocks that were polished down to expose areas for analysis in the SEM (Fig. 2A).

The SEM analyses in this paper sought not only to investigate sulfide impacts but also to determine the value of such initial investigations performed on Stardust craters. Therefore, residues had to be analyzed in-situ (matching real Stardust SEM analysis conditions). Although the SEM is capable of obtaining EDX data from crater residues with no need for sample preparation, the complicated geometry involved and the location of the EDX detector on this instrument (see section '2.3 Analytical Instrumentation and Sample Analysis') means that analyses are limited to a crescent-shaped region opposite the detector. These regions are located on the steep crater walls resulting in oblique beam-to-sample incidence. Such beam-sample incidence angles result in X-ray excitation from a very shallow volume and consequently relative enhancement of low-energy X-rays, preventing the use of available quantitative correction routines (Goldstein et al., 1992; Kearsley et al., 2007; Wozniakiewicz et al., 2009). However, Kearsley et al. (2007) noted that, if the foil is tilted directly toward the EDX detector, it is possible to collect X-rays emitted from the crater wall-to-floor arc, with beam-normal incidence on the residue enabling the successful application of correction routines. Fortuitously, these (deeper) locations tend to contain a higher abundance of residue (Kearsley et al., 2008). The

impact analogue foils were therefore dismounted from the base plates and fixed to an SEM stub which could then be mounted at an angle of 40° (the tilt required for this SEM) during EDX analyses (Fig. 2B).

In order to analyze samples by TEM, they must be prepared as electron transparent thin sections that are ~100 nm thick or less. Currently the preferred method available for creating these sections from large samples utilizes the focused ion beam (FIB) to extract sections typically 10 to 20 μm long by 10 μm deep. This preparation method is sensitive to the topography of the sample: The flat embedded projectiles are ideal; however, complex geometries like that of a crater cause complications to beam-sample interactions (with secondary ions and atoms being re-deposited elsewhere in the crater, covering and modifying existing residue) and make section extraction by micromanipulators impossible. For very small craters (with diameters of less than a few μm), infilling with carbon to create a flat geometry has enabled sections across whole craters to be made and analyzed (e.g. Leroux et al., 2006, 2008, 2010; Stroud 2010). However, larger craters like those investigated here cannot be infilled in this way and, to date, only sections taken from their well-exposed lips or the tops of their crater walls have been attempted (e.g. Graham et al., 2006, 2008). Given that the majority of residue is often found at the bottom of these craters (Kearsley et al., 2008), and that our SEM analyses were focused on these lower regions, it was vital that a sample preparation method be developed to enable access to these deeper regions by FIB. Hence, a section of each foil was mounted vertically within a resin block. These blocks were then polished down until a crater cross-section was revealed and residue was exposed at the surface Fig. 2C. Due to the non-conductive nature of these blocks, they required C-coating prior to SEM analyses. SEM EDX was then used to determine the location of outcropping residue for FIB.

2.3.   Analytical Instrumentation and Sample Analysis

All SEM imaging and EDX analyses for this investigation were conducted using the JEOL 5900 LV SEM in the Electron Microscopy and Mineral Analysis Division (EMMA) of the Department of Mineralogy at the Natural History Museum, London (NHM). An accelerating voltage of 20 kV, beam current of 2 nA and a working distance of 10 mm were used. BSE images, SE images and EDX microanalyses were obtained through an Oxford Instruments system, running version 16 INCA software. Before all compositional analyses, the X-ray microanalyser was calibrated with the acquisition of a 50 second spectrum from a cobalt standard. Point spectra were then acquired from the pre-impact projectiles and from 5 craters over 50 μm in diameter from each of the impact analogues. The atomic % data for the major element Kα lines (S, Fe and Ni) were then used for comparing precursor projectiles and resulting residues.

FIB sections were produced using FEI Nova600 NanoLab dual-beam FIB microscope at Lawrence Livermore National Laboratory (LLNL). They were then analyzed using the 200 kV FEI Tecnai T20 G2 field emission gun (FEG) monochromated scanning transmission electron microscope (STEM) at LLNL. Sections were imaged in bright field (BF) TEM and high angle annular dark field (HAADF) STEM. STEM-EDX atomic % data for the major element Kα lines was obtained for projectile and residue bulk chemistry comparisons, using k-factors that were evaluated against thin film mineral standards. STEM-EDX maps provided detailed chemical data for the highly complex residues. Electron diffraction patterns were used to determine crystal structures where possible.

3.   RESULTS AND DISCUSSION

3.1.   Initial SEM Analyses: Preservation of Chemistry

The SEM-EDX data obtained from pre- and post-impact pyrrhotite and pentlandite are plotted on separate ternary diagrams of S, Fe and Ni in atomic % (Fig. 3). The theoretical compositions of pyrrhotite and pentlandite in literature are given as $Fe_{(1-x)}S$ with $0<x<0.2$ and $(Fe,Ni)_9S_8$ respectively (Deer et al., 1992). Our quantitative SEM-EDX analyses of the pre-impact projectiles found that these particular samples had average compositions of $Fe_{(1-x)}S$ where $x=0.15$ (pyrrhotite) and $(Fe,Ni)S$ (pentlandite). Lines marking constant Fe to S, Ni to Fe and Ni to S ratios based on these average projectile compositions have been added to these ternaries.

The ternary diagrams (Fig. 3) show that pyrrhotite and pentlandite are easily distinguished as projectiles, and they have remained so as residues. The majority of the pentlandite residue data have maintained the original Fe to Ni ratio. However, these ternary diagrams echo that produced during the preliminary examination for the sulfide terminal grains in aerogel (Fig. 2 of Zolensky et al., 2006), with the majority of data for both minerals exhibiting varied degrees of loss of S. There are also a few data points that do not fit with these trends, being slightly enriched in Fe relative to Ni and vice versa (pentlandite), or slightly enriched in S relative to Fe and Ni (both pyrrhotite and pentlandite). These plots could highlight real changes in chemistry, however, there are several potential complications to the analyses that need to be taken into consideration. In a previous paper, the ability of the SEM to investigate in-situ the compositions of crater residues of a variety of silicate minerals was studied (Wozniakiewicz et al., 2009). Those analyses were performed without the foils being tilted towards the EDX detector, and were therefore subject to the effects of beam-sample incidence (as mentioned in section '2.2. Sample Preparation'), however, several further important factors were highlighted as having potential to complicate the relative counts (and therefore atomic %) detected. Those relevant to the present sulfide analyses are: secondary fluorescence (SF), target impurities, projectile impurities and gun-derived debris (GDD).

Secondary fluorescence (SF), the phenomenon whereby the X-rays generated by one element in the sample can stimulate the production of lower energy X-rays from the same sample (see description in Goldstein et al., 1992), is expected to occur between the elements that compose these sulfides, with Fe Kα X-rays generating S Kα X-rays and, in the pentlandite, Ni Kα X-rays generating both Fe and S Kα X-rays. Quantitative correction routines assume the sample is homogeneous to the extent of beam penetration and attempt to account for SF. However, residues are thin layers, and if their thickness is less than that of the beam penetration depth, then SF between their elements is reduced compared to that of a large mass. As a result, the quantitative correction routines will be overcompensating so that, when compared against projectile analyses, both residues may appear to be enhanced in higher energy X-rays. Those data points where Fe is increased relative to S for pyrrhotite, and where Ni is increased relative to S and Fe for pentlandite, may represent locations of thin residue (where SF is reduced and thus overcompensated).

The target Al 1100 foil contains discrete, randomly distributed Fe- and Si-rich inclusions typically a few microns in size (Kearsley et al., 2006). If an impact occurred over Fe-rich inclusions, they could lie beneath a residue (within the beam penetration depth) or even have mixed with the residue, adding to the Fe signal of an analysis. The Fe-rich inclusions could have contributed to both mineral residues, producing some of the pyrrhotite data with apparent decreases in S and the few data points for pentlandite that are high in Fe relative to S and Ni.

The impurities observed in the pre-impact samples were chalcopyrite (in pyrrhotite) and pyrrhotite (in pentlandite) (see Table 1). The lack of Cu signals in analyzed residue data suggests pyrrhotite impactors were pure. For the pentlandite, the low abundance of these

impurities meant there was a low probability of their occurrence in impactors, but their influence cannot be ruled out for those outliers high in Fe relative to S and Ni.

Gun-derived debris (GDD) is an impurity introduced to the samples by the LGG after the impact has occurred and is composed of cartridge powder, sabot, previous projectiles and targets, and material broken away from the inside of the gun itself (Wozniakiewicz et al., 2009). It results in a fine coating of C and a littering of larger particles which exhibit compositions that are C-rich or Fe- and Si-rich oxides, often with accompanying minor concentrations of Ca, Mn, Cu and Cl. The fine C-coating is unavoidable, however, great care was taken to steer clear of the larger particles during analysis. Although no signs of Si, Ca, Mn, Cu or Cl peaks were detected, we cannot be sure that the Fe oxide GDD were avoided in our analyses, and therefore these could be contributing to those data enhanced in Fe relative to S (and Ni).

The differences observed between these iron sulfide projectile and residue analyses could therefore be the result of multiple factors; real changes in chemistry, SF, target impurities, projectile impurities and GDD. (We note, however, that only the first three of this list are applicable to real Stardust impacts). To further investigate and qualify these, we look to the TEM analyses of the next section.

3.2. TEM Analyses: Preservation of Mineralogy

BF TEM images, diffraction patterns and EDX spectra were obtained from the projectiles to confirm homogeneity, initial crystallinity and composition. HAADF STEM images were obtained from residue sections, with differences in Z contrast between the resin, residue and foil enabling identification of areas of residue. EDX spectra were obtained to compare chemistry against that of the original projectile and also used together with EDX maps to highlight compositional homogeneity/heterogeneity. Electron diffraction patterns were obtained where possible to compare crystallinity against that of the initial projectile. Together these data enabled a direct comparison of projectile and residue.

The Pre-impact Projectiles
BF TEM images and diffraction patterns from the projectile sections are displayed in Fig. 4 and 5. The diffraction patterns were indexed as pyrrhotite (2H hexagonal pyrrhotite) and pentlandite. STEM-EDX spectra obtained from the projectile sections gave pyrrhotite compositions ranging from $Fe_{0.87}S$ to $Fe_{1.09}S$, with an average composition of $Fe_{1.02}S$ and pentlandite compositions ranging from $(Fe,Ni)_{1.27}S$ to $(Fe,Ni)_{1.48}S$ with an average composition of $(Fe,Ni)_{1.35}S$. These data are plotted on all ternary diagrams in Figs. 6B-D and 8B-F along with lines marking constant Fe to S, Ni to Fe and Ni to S ratios based on the average projectile compositions to enable comparisons with residue data. The TEM derived compositions are depleted in S relative to those determined by SEM-EDX. This depletion is caused by the FIB preparation technique, which sputters elements at different rates. The variation observed in the degree of S depletion for the TEM projectile sections is a result of differences in section thickness: the projectiles were prepared with a "knife edge", a progressive thinning toward the outside edge, and the amount of S-surface depletion is more significant in thinner regions. Knife edge preparation was employed to facilitate the interpretation of S content in our residues, where the multi-component nature (resin, foil, residue etc) leads to varied milling rates and therefore complicated, varied thicknesses that are difficult to judge. By measuring the compositions over a variety of projectile thicknesses, we aimed to identify the range in S content that could be attributable to section thickness thereby allowing us to distinguish impact generated changes in residue S content (the discussions below will only recognize changes in composition when data lie beyond the range of projectile compositions).

The Post- Impact Pyrrhotite Residue
The HAADF STEM image of the pyrrhotite residue section is shown in Fig. 6A. The Z contrast between the residue, resin and Al foil were sufficiently distinct to allow these components to be easily distinguished (see inset drawing of Fig. 6A). The pyrrhotite residue appears to be made up of four distinct components: Fractured blocks, high Z spheres, low Z spheres and fluffy material. In order to determine the nature of these components (composition, structure, genesis) electron diffraction patterns, STEM-EDX spectra and STEM-EDX elemental abundance maps were obtained. The results of analyses of the EDX spectra are displayed in the ternary diagrams of Al, S and Fe atomic % in Fig. 6B-D, and the individual EDX elemental abundance maps are displayed in Fig. 7.

Fractured Blocks: The bulk of the residue is in the form of blocky material that is bright in the HAADF STEM image against the resin and foil and has large fractures running throughout. Compositionally, the majority of this material matches the pre-impact projectile, although some data points, taken from the edges of these blocks, plot towards enrichment in Al (Fig. 6B). The interfaces between these blocks and the foil exhibit textures reminiscent of melting, suggesting the presence of a rim of material that began to melt and mix with the Al foil, thereby resulting in the varied Al content observed in such locations. The EDX element abundance maps (Fig. 7) also highlight this. Electron diffraction patterns taken from the main body of these blocks are well-indexed as pyrrhotite (2H hexagonal pyrrhotite) although there is some elongation of diffraction spots indicating shock.

High Z Spheres: Some residue takes the form of bright spheres lying above the bulk residue, either completely separate from these blocks or apparently frozen in the process of leaving them. These spheres exhibit varying amounts of Fe, Al and S (see EDX maps of Fig. 7), with S severely depleted relative to the original projectile (up to 7 atomic %, see Fig. 6C). These spheres are crystalline, however none of the patterns generated could be indexed to the pyrrhotite cell or known equilibrium Fe-Al alloys (probably due to the minor S content). These features are not GDD: the only GDD that would contain S would be remnants of previously shot iron sulfide projectiles which would exhibit such chemistries and diffraction patterns and, due to being prepared by crushing, would be angular and not spherical. Instead we appear to have generated impact melts which have crystallized into Fe-Al (+S) alloy spheres.

Low Z Spheres: Within some of these bright spheres were dark spheres. From the EDX maps (Fig. 7), these spheres appear to be dominated in composition by S. No STEM-EDX spectra were obtained solely from these spheres because they are too small (smaller than the section thickness). However, a single spectrum obtained from an area of a high Z (bright) sphere containing a low Z (dark) sphere exhibited slightly higher S content when compared to those analyses of the high Z spheres alone (the cross in Fig. 6C), suggesting that the dark sphere composition is S-rich. As they are small and encased in the Fe-Al alloy spheres, any diffraction patterns they might generate were masked.

*Fluffy Material: S*urrounding the bright spheres is an apparent 'fluffy' material. This fluffy material appears to have compositions dominated by O and C with minor Al, S and Fe (Fig. 6D and 7). The presence of C is not clear in the EDX abundance maps because the high C content of the resin has forced the contrast up, hiding its true extent in the fluffy material. Al, Fe and S were found to be present in at least a few atomic %, with Al exceeding 10 atomic % in most cases. In general, this material maintained the Fe to S ratio of pyrrhotite (Fig. 6D). No clear diffraction patterns could be obtained. This material is probably a mixture of very fine (nm-scale, therefore

unable to generate clear diffraction patterns) GDD, mixed with fragments of late impact ejecta with low energy rendering it unable to leave the crater.

In summary, the pyrrhotite residue appears to be made up of several components. The majority is in the form of fractured blocks which are pyrrhotite in composition and structure. The crystalline, Fe-Al alloy (high Z) spheres and S-rich (low Z) spheres are likely the result of melting, segregation and loss of more volatile S from Fe followed by mixing with molten Al foil. The areas of blocks at the foil-residue boundary that exhibit a molten texture represent the material at the front of the projectile that impacted first. This material experienced melting and mixing with Al, but may have been unable to lose S due to confinement by incoming material from the rear of the projectile. The fractured blocks are pyrrhotite projectile material that experienced fragmentation but remained structurally and chemically intact after impact. The pyrrhotite projectile therefore appears to have been largely preserved after impact, but some areas have experienced melting which has resulted in loss of S and the production of new phases, some of which may have increased their Fe content by incorporating target Fe-rich inclusions. Finally, the surface of the pyrrhotite residue is also littered with GDD (fluffy material).

The Post-Impact Pentlandite Residue
The HAADF STEM image of the pentlandite residue section is shown in Fig. 8A. The Z contrast between the residue, resin and Al foil are sufficiently distinct to allow these components to be easily distinguished (see inset drawing of Fig. 8A). Like the pyrrhotite, the pentlandite residue is also complex, taking the form of five different components: High Z spheres and blocks, low Z spheres, fluffy material, solid boundary material and diffuse boundary material. The nature of these components (composition, structure, genesis) was investigated be obtaining electron diffraction patterns, STEM-EDX spectra and STEM-EDX elemental abundance maps. The results of the EDX spectra are displayed in the ternary diagrams of S, Fe and Ni atomic % in Fig. 8B-F and the individual EDX elemental abundance maps are displayed in Fig. 9.

High Z Spheres and Blocks: The majority of the residue is in the form of bright spheres and blocks. The STEM EDX spectra (Fig. 8B) and maps (Fig. 9) show that these components are dominated by Fe, Al and Ni with minor S, with compositions typically containing around 30 atomic % Fe and Ni, 40 atomic % Al and up to a few atomic % S. Variation in the Al content is evident from feature to feature, although most maintain a close-to-original projectile Fe to Ni ratio after impact despite losing S (Fig. 8B). One sphere does, however, exhibit a very high Fe content, suggesting either varied partitioning of Fe and Ni, or the addition of Fe from an Fe-rich foil inclusion. These materials are all crystalline; however, none of the diffraction patterns obtained could be indexed to the pentlandite cell or any documented equilibrium Ni-Fe-Al alloy. This may be due to the minor S content. These diffraction patterns and Fe-, Al-, Ni-rich compositions suggest these are crystalline alloy spheres produced from impact-generated melts.

Low Z Spheres: The low Z spheres occur within high Z spheres and blocks. They are amorphous and typically enriched in S relative to Fe and Ni (see Fig. 8C and 9), with those closer to the original pentlandite Fe to S to Ni ratios being enriched in Al and O. The S-rich spheres are likely the result of capture of S released during impact, while the Al- and O-rich spheres share more affinity with the material of the fluffy masses (next section), possibly having been encased by the molten residue after impact, or simply appearing encased by the alloy in this particular two-dimensional section.

Fluffy Material: This fluffy material appears to have compositions dominated by O with moderate C and Al and minor S, Fe and Ni (see Fig. 8D and 9). The level of C- and Al- content is not

9

represented well in the EDX abundance maps because the high C-content of the resin and high Al-content of the foil increased the contrast, hiding their true abundance in the fluffy material. Ni, Fe and S are present at levels of at least a few atomic % and, although the fluffy material maintains a close-to-original pentlandite Ni to S ratio, it is enriched in Fe (Fig. 8D). This increased Fe content could indicate a GDD source for this material (which may not have caused a significant increase in Fe for the pyrrhotite fluffy masses as the level of contaminant within GDD changes with each shot). No clear diffraction patterns could be obtained. Like the fluffy material in the pyrrhotite residue section, this is probably a mixture of very fine GDD and fragments of late impact ejecta with low energy rendering it unable to leave the crater.

Solid Boundary Material and Diffuse Boundary Material: In the pentlandite residue section, the exact boundary between the residue and foil is not as clear as it is in the pyrrhotite residue. Instead, the boundary appears to be characterized by the remaining two components: a solid band of bright material and a diffuse band of bright material. The solid boundary material appears to be dominated by Al, Fe, Ni and, in one region, by S (Fig. 9). STEM-EDX spectra (Fig. 8E) show that the areas low in S are similar in composition to the high Z spheres and blocks, with Fe to Ni ratios close to the original pentlandite projectile. The region with more abundant S appears to have a bubbly texture, with dark areas possibly being minute, low-Z, S-bearing spheres. This material plots close to the original pentlandite S to Fe to Ni ratio. The diffuse boundary material appears to be dominated by Al with lesser amounts of Fe, Ni, and S. This material has largely maintained the Fe to Ni to S ratio of the original pentlandite projectile (most data occur within the range of possible (FIB-prepared) projectile compositions, Fig. 8F). It appears that the pentlandite may have melted, but rapidly combined with Al by the force of the impact, forming a rapidly quenched 'solid solution', thereby not allowing the segregation and loss of S to occur. Although diffraction spots indicated the presence of crystalline material in both solid and diffuse components, no clear single crystal patterns were obtained.

In summary, the pentlandite residue, like the pyrrhotite residue, appears to be made up of several components. Unlike the pyrrhotite residue, however, none of these components matched the pentlandite residue in structure and chemistry – all components appeared to be the result of melting, segregation, and loss of more volatile S, followed by mixing with molten Al foil. The majority of the residue is in the form of high Z spheres and blocks which are crystalline and composed of various Fe-Ni-Al alloys. Within these are amorphous S-rich spheres, captured during solidification of the alloy spheres and blocks. Both alloy spheres and S-rich spheres were also identified in the pyrrhotite residue. The solid boundary material appears to have similar compositions to the alloy spheres and blocks unless bubbles are present in which case major element ratios closer to the original pentlandite are observed. Like the material of the fractured block boundaries in the pyrrhotite residue, the diffuse boundary material represents the projectile material that impacted first and which, after melting, was forced into the Al foil by the rear of the projectile. This has resulted in the S remaining in the melt, giving an Fe to S to Ni ratio similar to pentlandite. Finally, the surface of the pentlandite residue is littered with GDD (fluffy material). The pentlandite projectile was therefore completely altered in the impact, melting, segregating, and mixing with molten Al foil, and resulting in the production of new phases. The majority of residue components do, however, maintain close to original Ni to Fe ratio and those that do not are likely to be the result of mixing with Fe-rich target inclusions (ignoring the fluffy materials which are likely GDD and therefore likely deposited after impact has occurred). Previous work on Stardust Al foils has shown the Fe-rich target inclusions to be abundant, variable in size and random in distribution. Therefore, the occurrence of this impact over an inclusion comes as no surprise as craters of this size have a high probability of interacting with several inclusions (c.f. the number of inclusions visible within a 50µm diameter circle on Fig. 4. in Kearsley et al. (2006) and Fig. 3 in Wozniakiewicz et al. (2009)). It is

interesting, however, that these results suggest that the degree of mixing with Fe-rich target inclusions is not uniform throughout a single crater residue and therefore likely depends on the size and number of inclusions impacted. It is clear these inclusions are a potential obstacle to deciphering all original iron sulfide compositions.

3.3.   Calculating Impact Parameters

To complement and clarify the results of the TEM analyses rough estimates of the impact parameters, peak pressure (P_{peak}), peak post shock temperature (T_{pps}) and cooling time, were calculated. These calculations require the input of experimental Hugoniot data for the projectile and target and various material properties of the projectile (e.g. heat capacity, thermal conductivity). The available data are limited for minerals, with the required experiments being biased towards materials of industrial and military importance. As a result, these calculations were only performed for the pyrrhotite shots into Al 1100 foil since adequate data were not available for pentlandite.

Peak Pressure (P_{peak}): To determine P_{peak}, the graphical method outlined in Melosh (1989) was used, whereby a plot of pressure (P) against particle velocity (u) is constructed from available Hugoniot data for the Al target (plotted forwards from u = 0 at P = 0) and the pyrrhotite projectile (plotted backwards from u = the impact velocity, 5.85 km s^{-1}, at P = 0). The point at which the two curves intersect corresponds to the P_{peak}. Hugoniot data was obtained from Marsh (1980) for the Al 1100 target and from Ahrens (1979) and Brown et al. (1984) for pyrrhotite. The P_{peak} calculated for this impact is ~85 GPa (to the nearest GPa). This value falls within the ranges estimated in previous publications for impacts at this speed (Melosh, 1989; Burchell and Kearsley, 2008)

Peak Post-Shock Temperature (T_{pps}): T_{pps} is the temperature of the decompressed shocked material that results from waste heat deposited after shock and release. We estimated this using the method described by Artemieva and Ivanov (2004) and Fritz et al. (2005). The peak post shock temperature (T_{pps}) is expressed as:

$$T_{PPS} = T_0 + \frac{u^2_{max} - 2E_R}{2C_P}$$
Eq. 1

where T_0 is the pre-shock temperature of the material (300 K), u_{max} is the maximum particle velocity experienced in the projectile (in m s^{-1}), E_R is the energy lost from the projectile during release from high pressure (in J) and C_P is the specific heat capacity of the projectile (in J kg^{-1} K^{-1}). u_{max} was determined from the plot of u against P to be 2590 m s^{-1}. The value of C_P for pyrrhotite is 50.6 J mol^{-1} K^{-1} or 625 J Kg^{-1} K^{-1} (derived from Grønvold and Stølen (1992) for Fe$_{0.875}$S). E_R can be approximated by assuming that release occurs along the Hugoniot curve and that the Hugoniot is adequately represented by a linear shock-particle velocity relationship:

$$U = c + su$$
Eq. 2

where U is the shock velocity and c and s are constants. In this case,

$$E_R = \frac{c}{s}\left(u_{max} + \frac{c}{s}\ln\frac{c}{U_{max}}\right)$$
Eq. 3

(Artemieva and Ivanov, 2004; Fritz et al., 2005), where U_{max} is the maximum shock velocity. Plotting values of U against u, taken from the Hugoniot data sources referenced previously, the c and s values derived for pyrrhotite are 3070 m s^{-1} and 1.5, respectively. Inserting these and u = u_{max} into Eq. 2 gives a U_{max} of 6990 m s^{-1} and therefore an E_R of 1.90 x 10^6 J.

Inserting these values of u_{max}, C_P and E_R into Eq. 1 gives a T_{pps} of 2600 K (to the nearest 100K).

Cooling Time: A crude estimate of characteristic cooling time can be made by simplifying the impact geometry to one dimension (1D), ignoring the effects of the surrounding foil and assuming the only method of heat transport is by conduction. In this case temperature decays exponentially, with a characteristic decay time τ defined as:

$$\tau = \frac{L^2}{\alpha} = \frac{\rho C_P L^2}{k}$$ Eq. 5

where L is the characteristic length scale of the cooling object and α is the thermal diffusivity (Turcotte and Schubert, 2002), which can be expressed as $\alpha = k/\rho C_P$, where k is the thermal conductivity (W m^{-1} K^{-1}) and ρ is the density (kg m^{-3}). For the pyrrhotite crater residues, L (thickness of residue) is assumed to be 5 μm (based on the images shown in Fig. 6), k is 3.53 W m^{-1} K^{-1} (Clauser and Huenges, 1995) and ρ is 4710 kg m^{-3} (average for pyrrhotite from Deer et al., 1992). This gives a decay time τ of 10^{-5} s. We emphasize that this calculation is severely limited by the fact that the material properties applied are for solid pyrrhotite, whereas we expect at least some of this material to be molten pyrrhotite, and by the simplifying assumption of 1D conductive cooling. However, as other cooling mechanisms will reduce cooling time, this estimate serves as a useful upper bound on cooling time.

The calculated impact parameters confirm that the uncompressed melting temperature of pyrrhotite, ~1373-1473 K (Vaughan and Craig, 1978), was significantly exceeded in those areas that experienced the P_{peak} and accounts for the melt-produced phases identified in the pyrrhotite residue TEM section. However, the peak shock pressures in a finite projectile are not experienced throughout the whole body, and the rear of the projectile is likely to be less heavily shocked resulting in the survival of some crystalline material. In addition, it appears that the melting, segregation of S, mixing with Al *and* crystallization exhibited by the pyrrhotite (and pentlandite) residues were not inhibited by the short cooling time (~10^{-5} s). Since melting of pyrrhotite results in production of new phases, and since the short cooling time has clearly not inhibited the segregation of pyrrhotite components, the fragmented pyrrhotite blocks identified in the pyrrhotite residue must be original preserved projectile. As previously noted, the data required for these impact parameter calculations are not available for pentlandite; however, assuming pentlandite has a similar T_{pps} as that determined for pyrrhotite, the more extensive melting exhibited could be a result of the fact that this material has a lower uncompressed melting temperature of ~1135 K (Kullerud, 1963). It is, however, possible that the slightly higher impact velocity for the TEM-analyzed pentlandite foil (6.21 km s^{-1}) may also have contributed to this difference.

4.   CONCLUSIONS

This work has used a combination of SEM and TEM to investigate the degree of preservation in the residues of two iron sulfides, pyrrhotite and pentlandite. The SEM results highlight a possible change in chemistry, but used alone, SEM could not distinguish and remove the contribution of secondary fluorescence (SF), gun-derived debris (GDD), and target and projectile impurities in these samples. TEM, however, was able to show that the structures and compositions exhibited by the pyrrhotite and pentlandite residues suggest a very complex reaction to the impact process. Both of these iron sulfide residues contain several impact-generated components that clearly indicate the projectile has undergone heating, melting, segregation and some loss of S from Fe (and Ni) and mixing with molten Al. On cooling, the new alloy components have crystallized and, in areas, have captured exsolved S. The process of melting, segregation of S, mixing with Al *and* crystallization was therefore clearly not inhibited

by the short cooling time ($\sim 10^{-5}$ s). The pyrrhotite section reveals that some of the projectile remains compositionally and structurally intact, albeit with some evidence of shock. The pentlandite impact has resulted in the complete destruction of the original projectile in the examined section, although the majority of its residue components retain roughly the original Ni to Fe ratio. Those with higher Fe content than the original projectile (ignoring 'fluffy material') are likely the result of mixing with Fe-rich foil inclusions. The 'fluffy material' identified in both residues likely corresponds to GDD, and likely arrived after impact and therefore did not contribute to the melt. (This material is also not applicable to real Stardust impacts). The foils have therefore been unable to collect iron sulfides without at least some alteration occurring, but unequivocal identification of the original preserved iron sulfides may be possible by TEM through the location of Al-free areas of iron sulfide (if they exist).

With this information, we see that at least some of the S depletion indicated by the SEM-EDX analyses represents real loss of this element (as opposed to artifacts of sample and analysis effects). In addition, those few data points that exhibit enhanced S relative to the original projectile can be explained as arising from an area containing trapped S (low Z spheres) while those richer in Fe could represent mixing with Fe-rich inclusions, or analyses including Fe-rich GDD. We do however note that none of the factors that could cause the observed variations in SEM-EDX derived residue chemistries can be quantified and corrected for. As a result, the original compositions of iron sulfide impactors cannot be determined from SEM-EDX analyses of their residues. The 'first impression' that the SEM does provide, along with a knowledge of alteration experienced by different minerals nevertheless allows informed decisions to be made about how best to further investigate a crater residue. In the majority of cases the Ni to Fe ratios have remained identical to that of the original impactor. Therefore, these elements may also be used to distinguish these minerals (in both SEM and TEM) and determine whether comet 81P/Wild 2 differs from CP IDPs in its iron sulfide content (although Fe-rich foil inclusions and GDD need to be borne in mind).

It is clear that in order to comprehensively determine the state of preservation and define the products of impact for Stardust crater residues, this combined SEM and TEM investigation should be extended to include all likely minerals that may have impacted the Stardust aluminum foil collector surfaces as well as appropriate analogues of amorphous materials. In addition, more complicated impactors with varied internal structure (containing fractures, pores, grain boundaries) and gross morphology (aggregates) should be considered as we note that while craters arising from mono-mineralic cometary dust grains have been identified on Stardust foils (e.g. Leroux et al., 2008), most craters appear to be the result of polymineralic cometary dust grains. The Stardust sample set is unique and unlikely to be repeated soon. This, combined with its proven ability to capture and preserve silicate residue, in some cases better than aerogel, means that the foil-collected material is exceptionably valuable, and it is vital that all efforts be made to enable its successful interpretation.

Acknowledgments

References

Ahrens T. J. 1979. Equations of state of iron sulphide and constraints on the sulphur content of the Earth. *Journal of Geophysical Research* 84:985-998.

Artemieva N., and Ivanov B. 2004. Launch of martian meteorites in oblique impacts. *Icarus* 171:84-101.

Bradley J. P. 2003. Interplanetary Dust Particles. In *Meteorites, Comets and Planets: Treatise on Geochemistry Volume 1* edited by A. M. Davis., executive editors H. D. Holland and K. K. Turekian. Oxford: Elsevier-Pergamon. pp. 690-711.

Brown J. M., Ahrens T. J., and Shampine D. L. 1984. Hugoniot data for pyrrhotite and the Earth's core. *Journal of Geophysical Research* 89:6041-6048.

Brownlee D. E., Tsou, P., Anderson, J. D., Hanner, M. S., Newburn, R. L., Sekanina, Z., Clark, B. C., Hörz, F., Zolensky, M. E., Kissel, J., McDonnell, J. A. M., Sandford, S. A., and Tuzzolino A. J. 2003. Stardust: Comet and interstellar dust sample return mission. *Journal of Geophysical Research (planets)* 108(E10):8111.

Brownlee D. E., Tsou P., Aléon J., Alexander C. M. O'D., Araki T., Bajt S., Baratta G. A., Bastien R., Bland P. A., Bleuet P., Borg J., Bradley J. P., Brearley A., Brenker F., Brennan S., Bridges. J. C., Browning N. D., Brucato J. R., Bullock E., Burchell M. J., Busemann H., Butterworth A., Chaussidon M., Cheuvront A., Chi M., Cintala M. J., Clark B. C., Clemett S. J., Cody G., Colangeli L., Cooper G., Cordier P., Daghlian C., Dai Z. R., D'Hendecourt L., Djouadi Z., Domingúez G., Duxbury T., Dworkin J. P., Ebel D. S., Economou T. E., Fakra S., Fairey S. A. J., Fallon S., Ferrini G., Ferroir T., Fleckenstein H., Floss C., Flynn G., Franchi I. A., Fries M., Gainsforth Z., Gallien J. –P., Genge M., Gilles M. K., Gillet P., Gilmour J., Glavin D. P., Gounelle M., Grady M. M., Graham G. A., Grant P. G., Green S. F., Grossemy F., Grossman J. N., Guan Y., Hagiya K., Harvey R., Heck P., Herzog G. F., Hoppe P., Hörz F., Huth J., Hutcheon I. D., Ignatyev K., Ishii H., Ito M., Jacob D., Jacobsen S., Jones S., Joswiak D., Jurewicz A., Kearsley A. T., Keller L. P., Khodja H., Kilcoyne A. L. D., Kissel J., Krot A., Langenhorst F., Lanzirotti A., Le L., Leshin L. A., Leitner J., Lemelle L., Leroux H., Liu M.-C., Luening K., Lyon I., MacPherson G., Marcus M. A., Marhas K., Marty B., Matrajt G., McKeegan K., Meibom A., Mennella V., Messenger K., Messenger S., Mikouchi T., Mostefaoui S., Nakamura T., Nakano T., Newville M., Nittler L. R., Ohnishi I., Ohsumi K., Okudaira K., Papanastassiou D. A., Palma R., Palumbo M. E., Pepin R. O., Perkins D., Perronnet M., Pianetta P., Rao W., Rietmeijer F. J. M., Robert F., Rost D., Rotundi A., Ryan R., Sandford S. A., Schwandt C. S., See T. H., Schlutter D., Sheffield-Parker J., Simionovici A., Simon S., Sitnitsky I., Snead C. J., Spencer M. K., Stadermann F. J., Steele A., Stephan T., Stroud R., Susini J., Sutton S. R., Suzuki Y., Taheri M., Taylor S., Teslich N., Tomeoka K., Tomioka N., Toppani A., Trigo-Rodríguez J. M., Troadec D., Tsuchiyama A., Tuzzolino A. J., Tyliszczak T., Uesugi K., Velbel M., Vellenga J., Vicenzi E., Vincze L., Warren J., Weber I., Weisberg M., Westphal A., Wirick S., Wooden D., Wopenka B., Wozniakiewicz P. J., Wright I., Yabuta H., Yano H., Young E. D., Zare R. N., Zega T., Ziegler K., Zimmermann L., Zinner E., and Zolensky M. 2006. Comet 8P/Wild 2 Under a Microscope. *Science* 314:1711-1716.

Burchell M. J., Cole M. J., McDonnell J. A. M., and Zarnecki J. C. 1999. Hypervelocity impact studies using the 2 MV Van de Graaff dust accelerator and two stage Light Gas Gun of the University of Kent at Canterbury. *Measurement Science and Technology* 10: 41-50.

Burchell M. J., Fairey S. A. J., Wozniakiewicz P. J., Brownlee D. E., Hörz F., Kearsley A. T., See T. H., Tsou P., Westphal A., Green S. F., Trigo-Rodríguez J. M., and Domingúez G. 2008a. Characteristics of cometary dust tracks in Stardust aerogel and laboratory calibrations. *Meteoritics and Planetary Science* 43:23-40.

Burchell M. J., Foster N. J., Kearsley A. T., and Creighton J. A. 2008b. Identification of mineral impactors in hypervelocity impact craters in aluminum by Raman spectroscopy of residues. *Meteoritics and Planetary Science* 43:135-142.

Burchell M. J., and Kearsley A. T. 2009. Short-period Jupiter family comets after Stardust. *Planetary & Space Science* 57:1146-1161.

Christoffersen R., and Buseck P. R. 1986. Mineralogy of interplanetary dust particles from the "olivine" infrared class. *Earth and Planetary Science Letters* 78:53-66.

Clauser C., and Huenges E. 1995. Thermal conductivity of rocks and mineral. In *Rock Physics and Phase Relations: A Handbook of Physical Constants* edited by T. J. Ahrens. Washington: American Geophysical Union Reference Shelf 3. pp 105-126.

Dai Z. R., and Bradley J. P. 2001. Iron-nickel sulfides in anhydrous interplanetary dust particles. *Geochimica et Cosmochimica Acta* 65:3601-3612.

Deer W.A., Howie R.A., and Zussman J. 1992. An introduction to the rock-forming minerals, 2nd edition. Harlow: Pearson Education Limited.

Fraundorf P. 1981. Interplanetary dust in the transmission electron microscope: diverse materials from the early solar system. *Geochimica et Cosmochimica Acta* 45:915-943.

Fritz J., Artemieva N. and Greshake A. 2005. Ejection of Martian meteorites. *Meteoritics and Planetary Science* 40:1393-1411.

Goldstein J. I., Newbury D. E., Echlin P., Joy C. D., Romig A. D. Jr., Lyman C. E., Fiori C., and Lifshin E. 1992. *Scanning Electron Microscopy and X-ray Microanalysis*, 2nd Edition. New York and London: Plenum Press.

Graham G. A., Kearsley A. T., Wright I. P., Grady M. M., Drolshagen G., McBride N. M., Green S. F., Burchell M. J., Yano H., and Elliott R. 2001. Analysis of Impact Residues on Spacecraft Surfaces: Possibilities and Problems, *In: Proceedings of the Third European Conference on Space Debris,* ESA Special Publication 473:197-203.

Graham G. A., Teslich N., Dai Z. R., Bradley J. P., Kearsley A. T., and Hörz F. 2006. Focused ion beam recovery of hypervelocity impact residue in experimental craters on metallic foils. *Meteoritics and Planetary Science* 41:159-165.

Graham G.A., Teslich N. E., Kearsley A. T., Stadermann F. J., Stroud R. M., Dai Z., Ishii H. A., Hutcheon I. D., Bajt S., Snead C. J., Weber P. K. and Bradley J. P. 2008. Applied focused ion beam techniques for sample preparation of astromaterials for integrated nanoanalysis. *Meteoritics and Planetary Science* 43:561-569.

Grønvold F., and Stølen S. 1992. Thermodynamics of iron sulfides II. Heat capacity and thermodynamic properties of FeS and of $Fe_{0.875}S$ at temperatures from 298.15 K to 1000 K, of $Fe_{0.98}S$ from 298.15 K to 800 K, and of $Fe_{0.89}S$ from 298.15 K to about 650 K. Thermodynamics of formation. *The Journal of Chemical Thermodynamics* 24:913-936.

Ishii H. A., Brennan S., Bradley J. P., Pianetta P., Kearsley A. T. and Burchell M. J. 2008a. Sulfur mobilization in Stardust impact tracks (abstract #1561). *39th Lunar and Planetary Science Conference.* CD-ROM.

Ishii H. A., Bradley J. P., Dai Z. R., Chi M., Kearsley A. T., Burchell M. J., Browning N. D. and Molster F. 2008b. Comparison of Comet 81P/Wild 2 dust with interplanetary dust from comets. *Science* 319:447-450.

Kearsley A.T., Burchell M.J., Hörz F., Cole M.J., and Schwandt C.S., 2006. Laboratory simulation of impacts on aluminium foils of the Stardust spacecraft: Calibration of dust particle size from comet Wild-2. *Meteoritics and Planetary Science* 41:167-180.

Kearsley A. T., Graham G. A., Burchell M. J., Cole M. J., Dai Z. R., Teslich N., Bradley J. P., Chater R., Wozniakiewicz P. J., Spratt J., and Jones. G. 2007. Analytical scanning and transmission electron microscopy of laboratory impacts on Stardust aluminium foils: Interpreting impact crater morphology and the composition of impact residues. *Meteoritics & Planetary Science* 42:191-210.

Kearsley A. T. Borg J., Graham G. A., Burchell M. J., Cole M. J., Leroux H., Bridges J. C., Hörz F., Wozniakiewicz P. J., Bland P. A., Bradley J. P., Dai Z. R., Teslich N., See T., Hoppe P., Heck P. R., Huth J., Stadermann F. J., Floss C., Marhas K., Stephan T., and Leitner J. 2008. Dust from comet Wild 2: Interpreting particle size, shape, structure and composition from impact features on the Stardust aluminium foils. *Meteoritics and Planetary Science* 43:41-74.

Kearsley A. T., Burchell M. J., Price M. C., Graham G. A., Wozniakiewicz P. J., and Cole M. J. 2009. Micrometeoroid impacts on spacecraft: Can asteroidal and cometary dust be distinguished? In *Proceedings of the 5th European Conference on Space Debris, ESA SP-672, Darmstadt, 30.3.-2.4.2009* (CD-ROM).

Kullerud G. 1963. Thermal stability of pentlandite. *The Canadian Mineralogist* 7:353-366.
Lauretta D. S., Lodders K., Fegley Jr. B., and Kremser D. T. 1997. The origin of sulphide-rimmed metal grains in ordinary chondrites. *Earth and Planetary Science Letters* 151:289-301.

Leroux H., Borg J., Troadec D., Djouadi Z., and Hörz F. 2006. Microstructural study of micron-sized craters simulating Stardust impacts in aluminium 1100 targets. *Meteoritics and Planetary Science* 41:181-196.

Leroux H., Stroud R. M., Dai Z. R., Graham G. A., Troadec D., Bradley J. P., Teslich N., Borg J., Kearsley A. T., and Hörz F. 2008. Transmission electron microscopy of cometary residues from micron-sized craters in the Stardust Al foils. *Meteoritics and Planetary Science* 43:143-160.

Leroux H., Kearsley A. T., and Troadec D. 2010. Mineralogy of Wild 2 residues in micron-sized craters from the Stardust Al-foils. (abstract #1621) *41st Lunar and Planetary Science Conference.* CD-ROM.

Lodders K. 2003. Solar system abundances and condensation temperatures of the elements. *The Astrophysical Journal* 591:1220-1247.

Marsh S. P. 1980. LASL Shock Hugoniot Data. Los Angeles: University of California Press. 674p.

Melosh H. J. 1989. *Impact Cratering – A Geologic Process*. New York: Oxford University Press.

Price M. C., Kearsley A. T., Burchell M. J., Hörz F., Borg J., Bridges J. C., Cole M. J., Floss C., Graham G., Green S. F., Hoppe P., Leroux H., Marhas K. K., Park N., Stroud R., Stadermann F. J., Teslich N., and Wozniakiewicz P. J. Comet 81P/Wild 2: The size distribution of finer (sub 10-micrometre) dust collected by the Stardust spacecraft. *Meteoritics and Planetary Science* In Press.

Stroud R. M., Kock I. M., Bassim N. D., Piccard Y. N., and Nittler L. R. 2010. Structure and composition of comet Wild 2 residues in sub-micron to micron-sized craters (abstract #1792). *41st Lunar and Planetary Science Conference.* CD-ROM.

Tsou P., Brownlee D. E., Sandford S. A., Hörz F., and Zolensky M. E. 2003. Wild-2 and interstellar sample collection and Earth return. *Journal of Geophysical Research (Planets)* 108(E10):8113.

Turcotte D. L., and Schubert G. 2002. Heat Transfer. In *Geodynamics*, 2nd edition. Cambridge University Press. 528p.

Vaughan D. J., and Craig J. R. 1978. Sulphide Phase Equilibria. In *Mineral chemistry of metal sulphides*. Cambridge University Press. pp 261-314.

Wozniakiewicz P. J., Kearsley A. T., Burchell M. J., Foster N. J., Cole M. J., Bland P. A. and Russell S. A. R. (2009) Analysis of residues resulting from laboratory impacts into aluminum 1100 foil: implications for Stardust crater analyses. *Meteoritics & Planetary Science* 44:1541-1559.

Zolensky M. E., and Thomas K. L. 1995. Iron and iron-nickel sulfides in chondritic interplanetary dust particles. *Geochimica and Cosmochimica Acta* 59:4707-4712.

Zolensky M. E., Pieters C., Clark., and Papike J. J. 2000. Small is beautiful: The analysis of nanogram-sized astromaterials. *Meteoritics & Planetary Science* 35:9-29.

Zolensky M. E., Zega T. J., Yano H., Wirick S., Westphal A. J., Weisberg M. K., Weber I., Warren J. L., Velbel M. A., Tsuchiyama A., Tsou P., Toppani A., Tomioka N., Tomeoka K., Teslich N., Taheri M., Susini J., Stroud R., Stephan T., Stadermann F. J., Snead C. J., Simon. S. B., Simionovici. A., See. T. H., Robert F., Rietmeijer. F. J.M., Rao W., Perronnet M. C., Papanastassiou D. A., Okudaira K., Ohsumi K., Ohnishi I., Nakamura-Messenger K., Nakamura T., Mostefaoui S., Mikouch T., Meibom A., Matrajt G., Marcus M. A., Leroux H., Lemelle L., Le L., Lanzirotti A., Langenhorst F., Krot A. N., Keller L. P., Kearsley A. T., Joswiak D., Jacob D., Ishii H., Harvey R., Hagiya K., Grossman L., Grossman J. N., Graham. G. A., Gounelle M., Gillet. P., Genge. M. J., Flynn. G., Ferroir. T., Fallon. S., Ebel D. S., Dai Z. R., Cordier P, Clark B., Chi M., Butterworth A. L., Brownlee D. E., Bridges J. C., Brennan S., Brearley A., Bradley J. P., Bleuet P., Bland P. A., and Bastien R. 2006. Mineralogy and petrology of comet 81P/Wild 2 nucleus samples. *Science* 314:1735-1739.

Tables, Figures and captions

Shot(s)	Projectiles (NHM sample)	Projectile size and shape	Impact speed (km s^{-1}) ± 2%	Inherent contaminants
G080507#3	Pyrrhotite (BM.2005,M317)	<53 µm irregular	5.82	Chalcopyrite
G291106#2 G2205072	Pentlandite (specimen awaiting cataloguing)	<53 µm irregular	5.85 6.21	Pyrrhotite inclusions

Table 1: Details of projectiles and parameters for two stage light gas gun (LGG) shots performed and analyzed as part of the work in this paper.
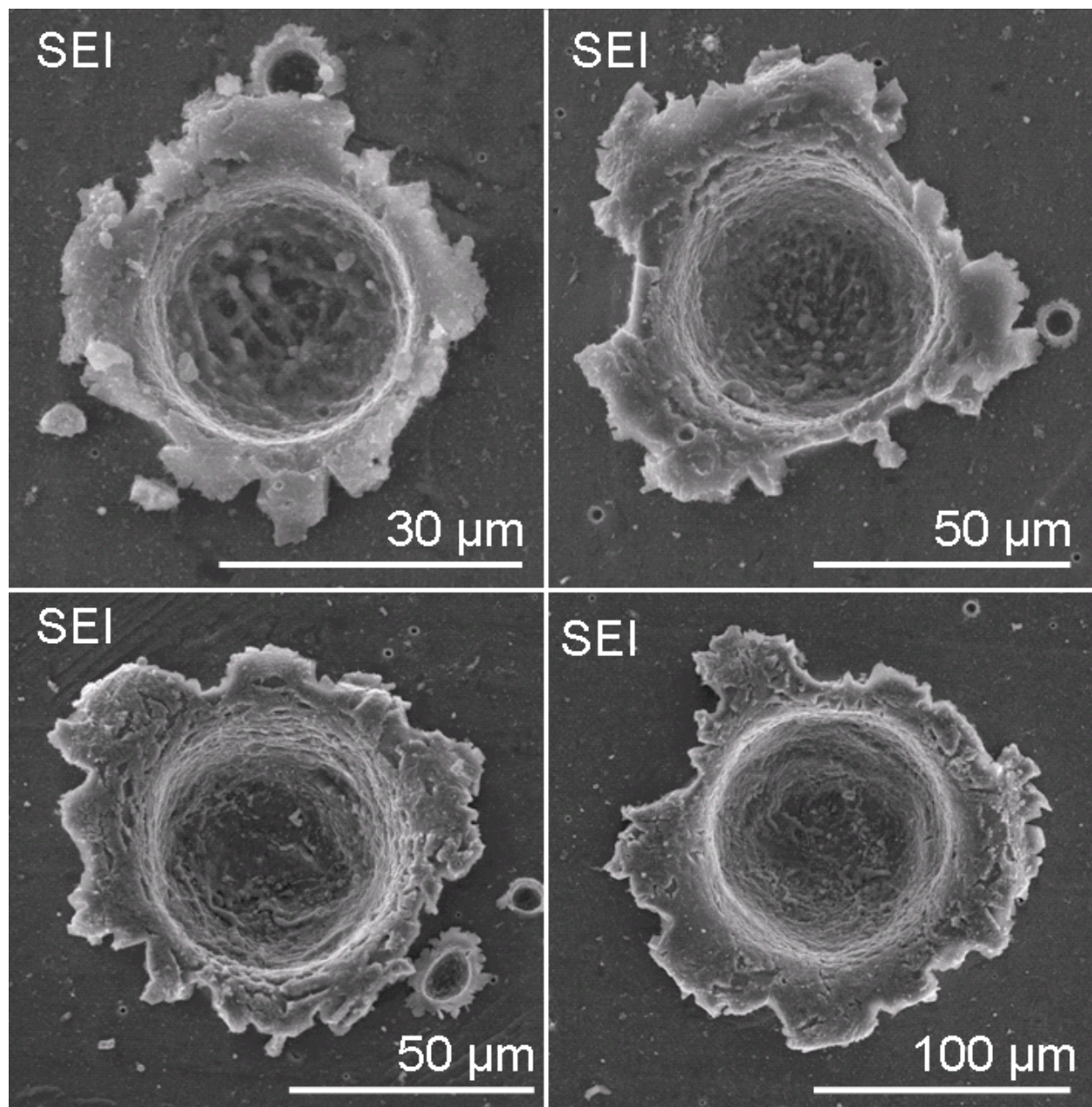
Figure 1: Secondary electron images of four impact craters. These were generated in the laboratory using the light gas gun to impact pyrrhotite into Stardust flight spare Al foils. The impacting particles are preserved in the form of residues that line the impact crater. This residue material appears as roughness in the surface of the crater.
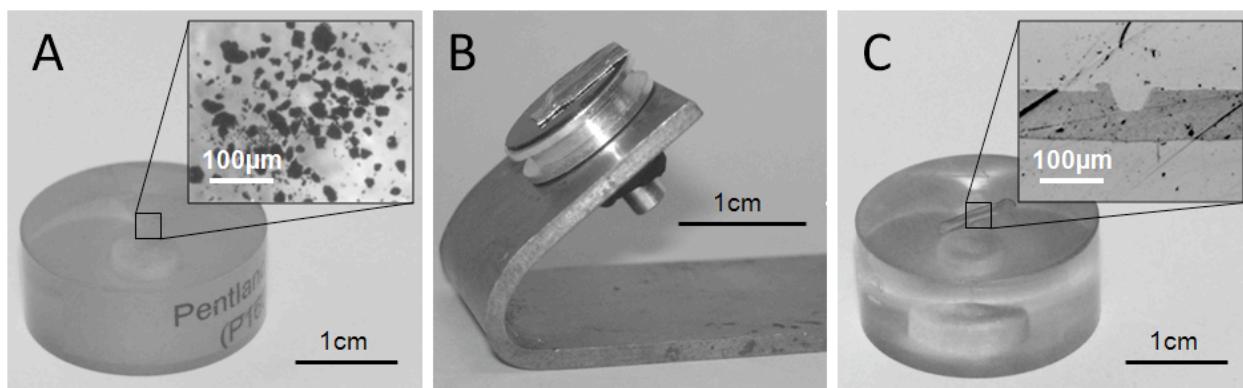
Figure 2: Preparation of pre- and post-impact analogue samples for SEM analysis and FIB preparation. A: Pre-impact projectiles were embedded in epoxy to enable quantitative analysis by SEM-EDX and TEM section preparation by FIB. B: Impacted foils were mounted on SEM stubs and tilted to facilitate quantitative SEM-EDX analyses. C: Impacted foils were embedded in epoxy and polished down until impact crater cross sections (and residue) outcropped on the surface to enable TEM section preparation by FIB. The inset in C shows a crater with residue in cross section at the epoxy surface.
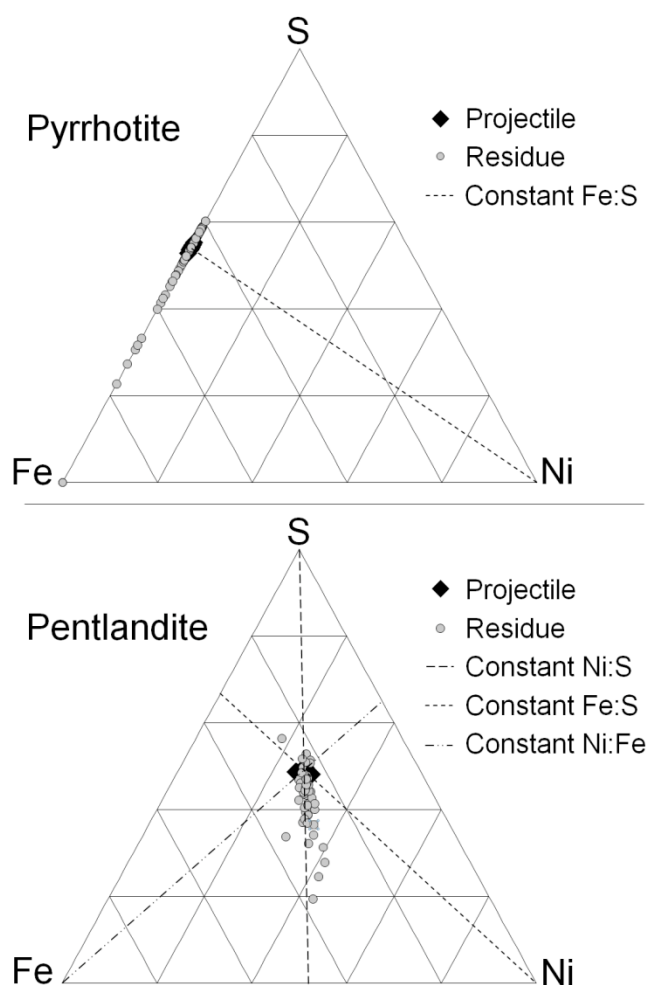
Figure 3: SEM-EDX atomic percentage data taken from pre- and post-impact samples (projectile and residue) of the sulfides A: Pyrrhotite and B: Pentlandite. Data for both residues were taken from tilted foils (Fig. 2B) to facilitate the extraction of quantitative atomic % data using available correction routines.
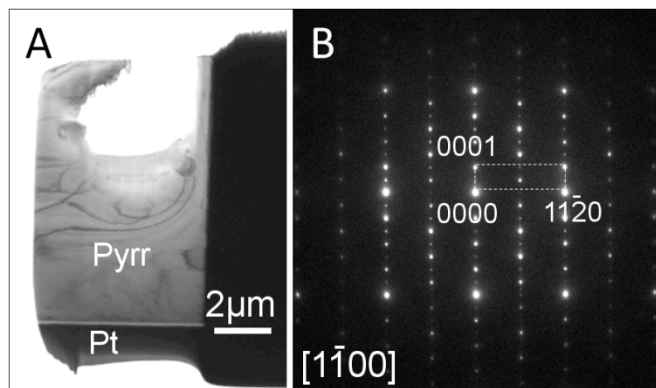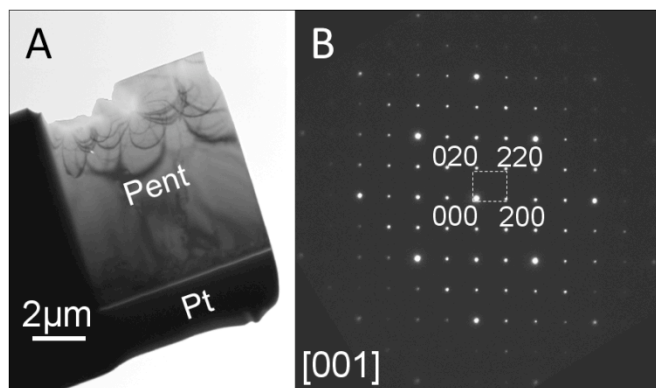

Figure 4: Pyrrhotite pre-impact projectile TEM section. A: Bright field TEM image of TEM section with protective Pt strap (Pt) and pyrrhotite (Pyrr). B: Diffraction pattern taken from section, indexed to hexagonal pyrrhotite cell, confirming crystallinity and pyrrhotite mineralogy.

Figure 5: Pentlandite pre-impact projectile TEM section. A: Bright field TEM image of section with protective Pt strap (Pt) and pentlandite (Pent). B: Diffraction pattern taken from section, indexed to pentlandite cell, confirming crystallinity and pentlandite mineralogy.
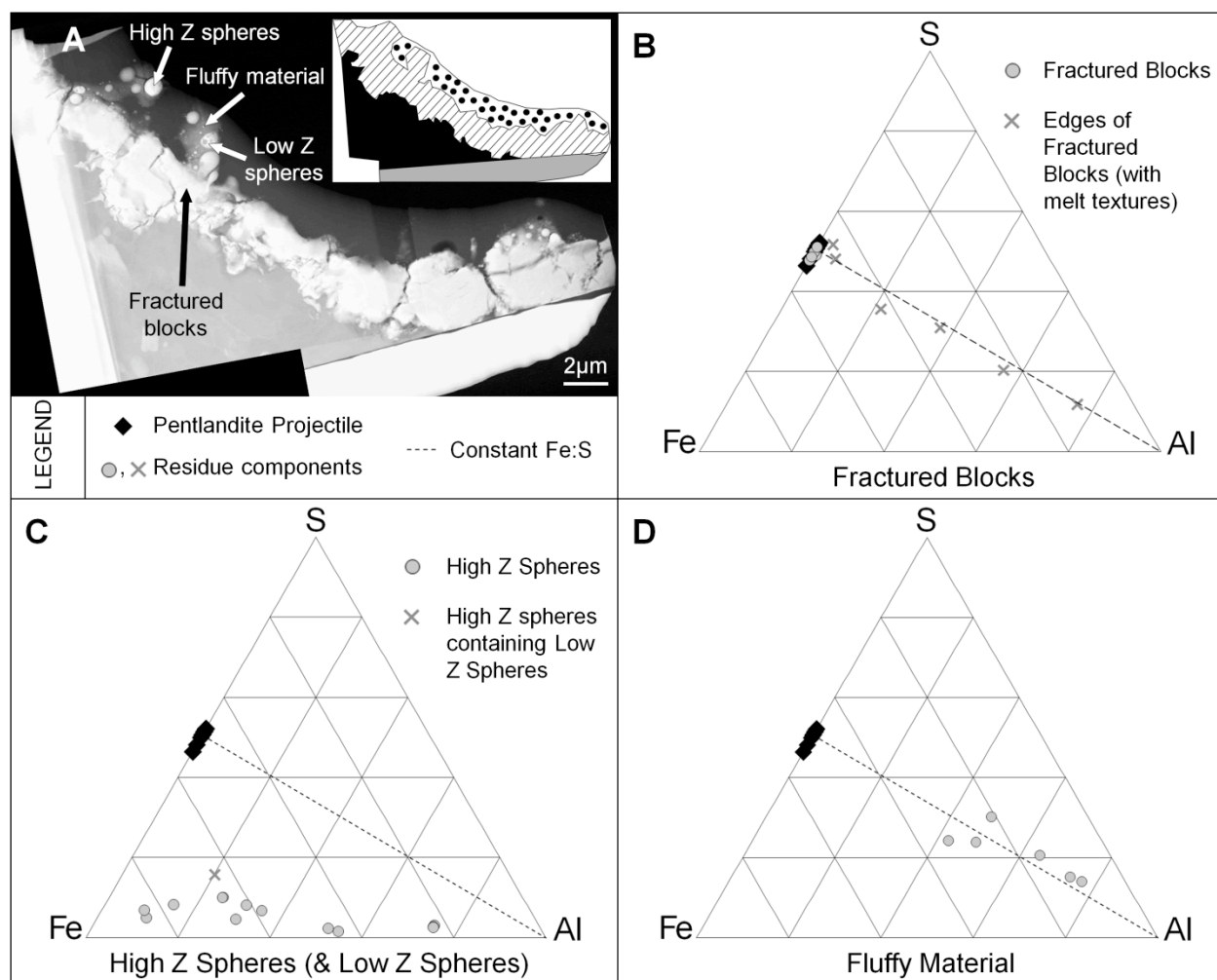
Figure 6: HAADF STEM image and STEM-EDX analyses of the pyrrhotite residue section. A: HAADF STEM image with inset drawing identifying the Al foil (black), protective Pt strap from the FIB extraction process (grey), embedding resin (spotty) and the residue (striped). Individual components of the residue are labeled. B-D: Ternary diagrams of S, Fe and Ni atomic percentage data from the STEM-EDX analyses for each of the individual components identified in the HAADF STEM image.
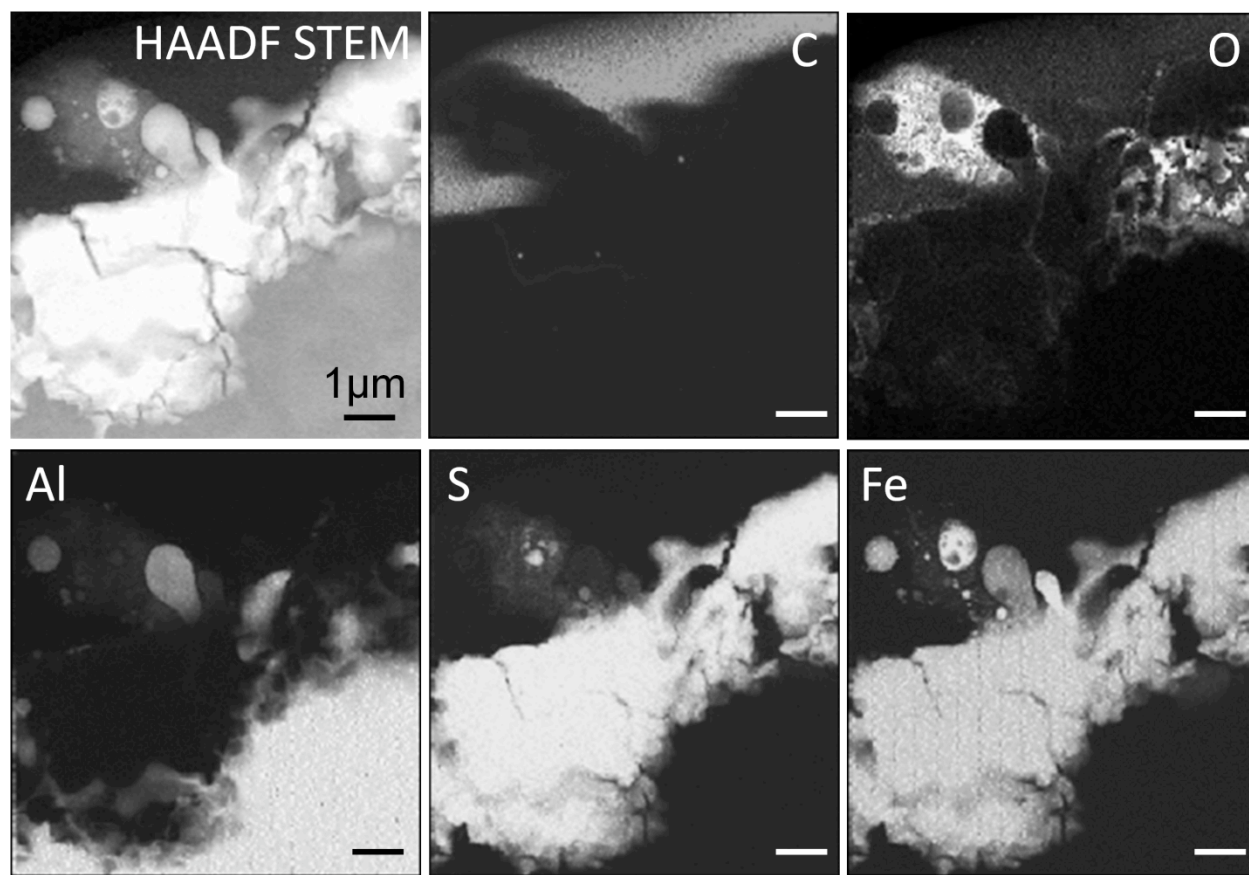
Figure 7: Elemental abundance maps from Kα x-rays of C, O, Al, S and Fe taken over the pyrrhotite residue section. Top left is the HAADF STEM image of this region. All scale bars represent 1µm.
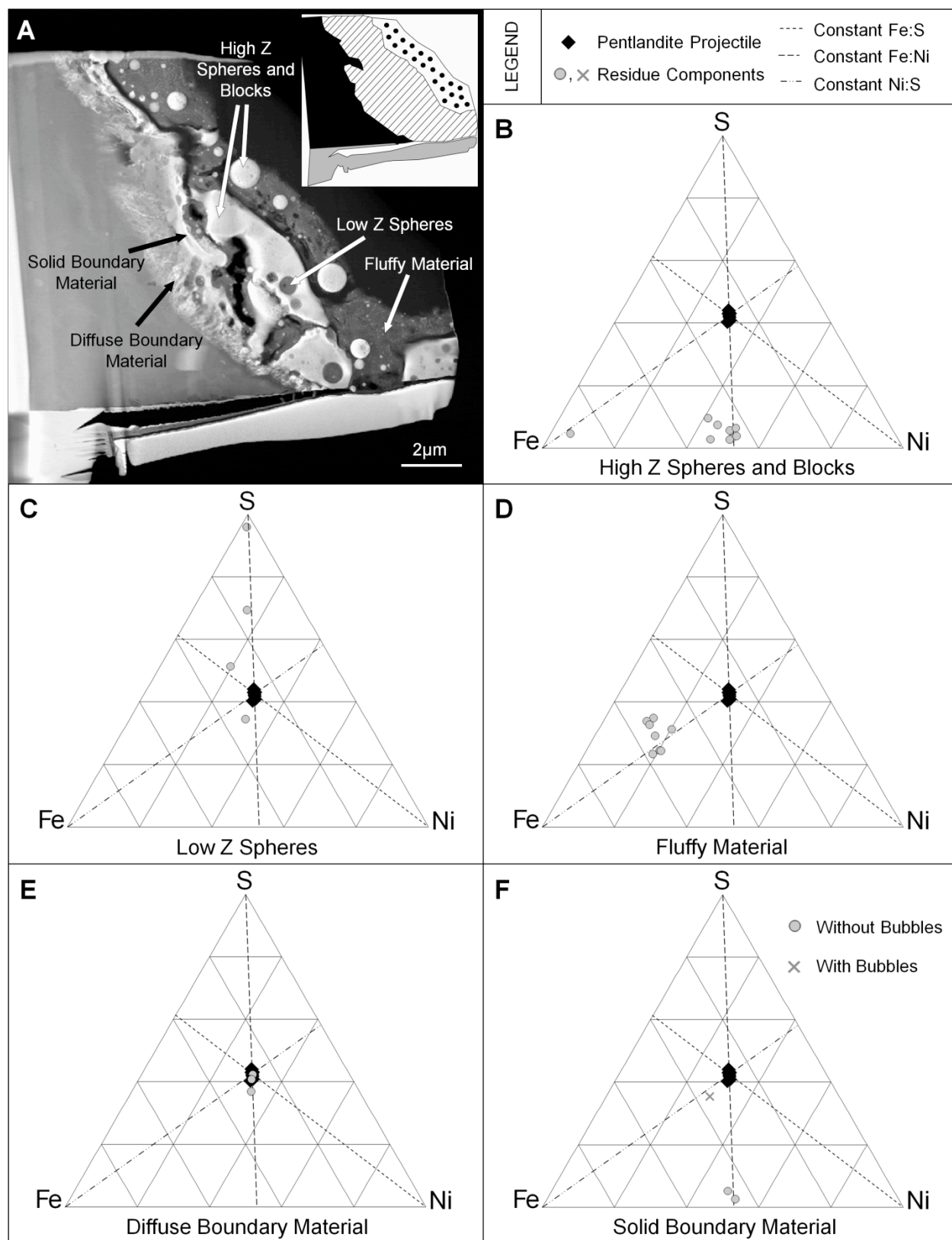
Figure 8: HAADF STEM image and STEM EDX analyses of the pentlandite residue section. A: HAADF STEM image with inset drawing identifying the Al foil (black), protective Pt strap from

the FIB extraction process (grey), embedding resin (spotty) and the residue (striped). Individual components of the residue are labeled. B-F: Ternary diagrams of S, Fe and Ni atomic percentage data from the STEM EDX analyses for each of the individual components identified in the HAADF STEM image.
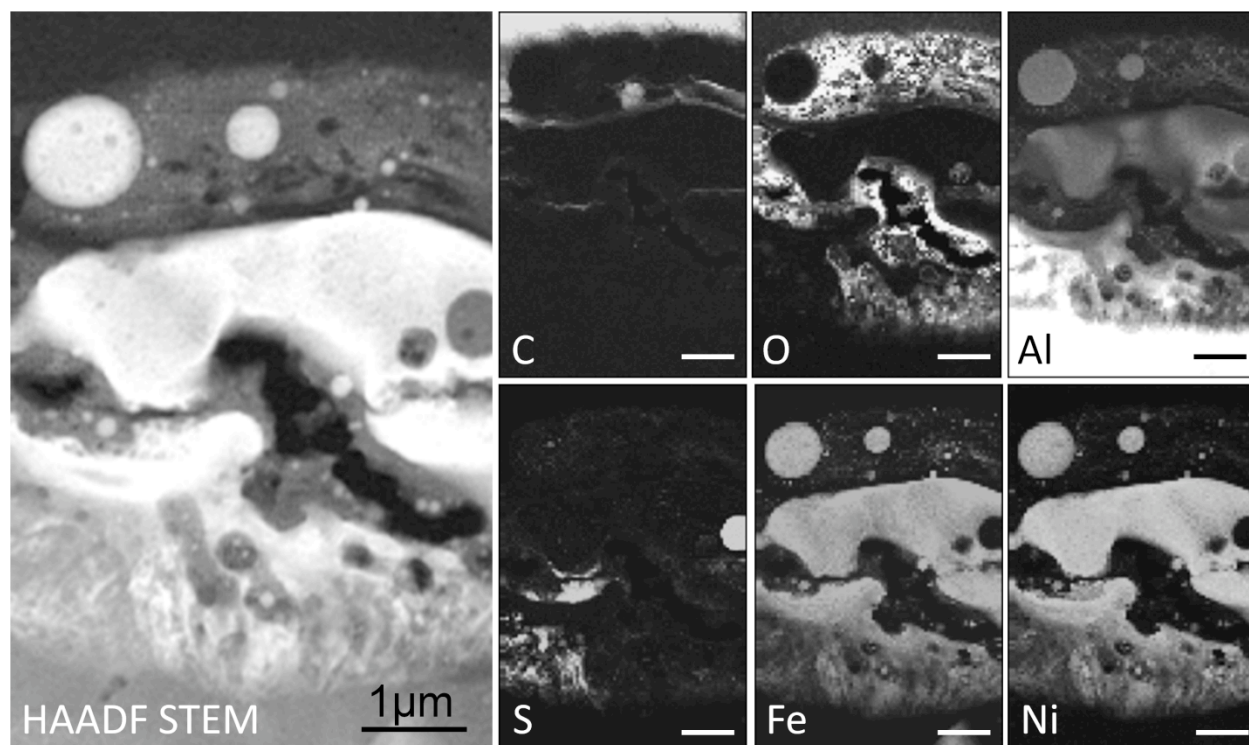

Figure 9: Elemental abundance maps from Kα x-rays of C, O, Al, S, Fe and Ni taken over the pentlandite residue section. Left is the HAADF STEM image of this region. All scale bars represent 1µm.